JAMES | Journal of Advances in Modeling Earth Systems

RESEARCH ARTICLE
10.1029/2020MS002336

The Effects of Ice Floe-Floe Interactions on Pressure Ridging in Sea Ice

A. Damsgaard[1,2], **O. Sergienko**[1], **and A. Adcroft**[1]

[1]Program in Atmospheric and Oceanic Sciences, Princeton University, Princeton, NJ, USA, [2]Now at Department of Geoscience, Aarhus University, Aarhus, Denmark

Key Points:

- Ice elasticity can provide large resistance during early compression of sea-ice floes
- Sea-ice deformation becomes spatially localized at the onset of ridging due to contact weakening
- We develop a mathematical framework for simulating the observed sea-ice ridging in large-scale sea-ice models

Correspondence to:
A. Damsgaard,
anders@adamsgaard.dk

Citation:
Damsgaard, A., Sergienko, O., & Adcroft, A. (2021). The effects of ice floe-floe interactions on pressure ridging in sea ice. *Journal of Advances in Modeling Earth Systems*, *13*, e2020MS002336. https://doi.org/10.1029/2020MS002336

Received 17 SEP 2020
Accepted 9 JUN 2021

Abstract The mechanical interactions between ice floes in the polar sea-ice packs play an important role in the state and predictability of the sea-ice cover. We use a Lagrangian-based numerical model to investigate such floe-floe interactions. Our simulations show that elastic and reversible deformation offers significant resistance to compression before ice floes yield with brittle failure. Compressional strength dramatically decreases once pressure ridges start to form, which implies that thicker sea ice is not necessarily stronger than thinner ice. The mechanical transition is not accounted for in most current sea-ice models that describe ice strength by thickness alone. We propose a parameterization that describes failure mechanics from fracture toughness and Coulomb sliding, improving the representation of ridge building dynamics in particle-based and continuum sea-ice models.

Plain Language Summary Considerable areas of the polar oceans are covered by sea ice, formed by frozen sea water. The extent and thickness of the ice pack influences local and regional ecology and climate. The ice thickness is particularly important for the ice-cover survival during warm summers. Wind and ocean currents compress and shear the sea ice, and can break and stack ice into ridges. Current sea ice models assume that the ice becomes increasingly rigid as ridges of ice rubble grow. Modeling sea ice as bonded particles, we show that ice becomes significantly weaker right after the onset of ridge building. We introduce a mathematical framework that allows these physical processes to be included in large-scale models.

1. Introduction

The presence of sea ice in the polar oceans has a profound effect on ocean-atmosphere interaction and global climate (e.g., Chiang & Bitz, 2005; Curry et al., 1995; Screen & Simmonds, 2010). The thickness of the sea-ice cover is a key factor controlling the summer sea-ice extent (e.g., Bushuk et al., 2017; Day et al., 2014; Lindsay et al., 2008), but remains difficult to observe remotely and predict accurately with numerical sea-ice models (e.g., Blanchard-Wrigglesworth et al., 2016; Haas, 2003; Holland et al., 2010). Internal stresses in sea ice floes and drag from the ocean and atmosphere can build up ice in thick ridges under compression, or form leads during extension that increase ocean-atmosphere energy exchange (e.g., Batrak & Müller, 2018; Haas, 2003; Parmerter & Coon, 1973; Thorndike et al., 1975). During ice rafting, one ice floes overrides another with limited brittle failure (e.g., Hopkins et al., 1999; Parmerter, 1975; Tuhkuri & Lensu, 2002). Ice ridging, a different deformation mode, occurs when ice floes break into smaller pieces and create a chaotic and thick rubble (e.g., Hopkins, 1998, 1994). The subaerial ice rubble produced by the ridging process is called a sail, and the subaqueous part a keel. Due to the difference in ice and water density, sea ice keels are deeper than their corresponding sails. It is crucial to understand ridging, as it provides the fundamental control on the ice-thickness distribution (e.g., Thorndike et al., 1975). The ice thickness distribution of real ice packs shows an exponential decrease with thickness due to ridging (e.g., Godlovitch et al., 2011; Toppaladoddi & Wettlaufer, 2015). Furthermore, the presence of keels and sails increase the form drag of the ice pack against ocean and atmosphere (Tsamados et al., 2014).

The study of ice strength is motivated not only by the perspective of sea-ice modeling, but also from the need to understand ice clogging of rivers, lakes, and marine passages (e.g., Damsgaard et al., 2018; Herman, 2013; Rallabandi et al., 2017; Shen & Liu, 2003), and mechanical resistance and wear against ships and other artificial structures (e.g., Heinonen, 2004; Timco et al., 2000). Coulomb failure is a general and scale-independent measure of ice strength (e.g., Weiss & Schulson, 2009), and has served as the constitutive basis for a range of

mechanical analyses. Mellor (1980) constrained analytical solutions for the mechanical resistance felt by simple ship-like geometries moving through brash ice with Mohr-Coulomb plasticity. The role of ice thickness on ridging and rafting processes was investigated in laboratory experiments by Tuhkuri and Lensu (2002). They found that the ice-thickness ratio, and not the absolute thickness, was the dominant parameter that determined whether sea ice undergoes ridging versus rafting. Small differences in ice-floe thicknesses tended to result in rafting with relatively little plastic failure, while ice floes with very different thickness experienced intense failure and ice ridge formation during compression. Furthermore, they observed that the compressional strain had to exceed an initial threshold value with linear resistance before actual ridging started. However, the resistive forces during ridging appeared to follow a non-linear relationship.

In most widely used large-scale continuum sea-ice models, the ice pack in each cell is described by thickness distribution functions (e.g., Flato & Hibler, 1995; Lipscomb et al., 2007; Thorndike et al., 1975; Ungermann et al., 2017). Ridge building modifies the thickness distribution, and is determined by the required increase in potential energy and associated frictional losses (Coon, 1974; Hopkins et al., 1991; Hopkins, 1998; Pritchard, 1975; Roberts et al., 2019; Rothrock, 1975). The ice strength is parameterized to scale with ice thickness (e.g., Hibler, 1979; Lipscomb et al., 2007). However, current ridge-building models lead to biases in the ice-thickness distribution, compared to observations (e.g., Amundrud et al., 2004; Flato & Hibler, 1995; Ungermann et al., 2017). Fractures in the sea-ice cover are known to relax internal stresses (Dansereau et al., 2016, 2017), and inclusion of resultant brittle deformation in large-scale models improves the correspondence between model and observations (Girard et al., 2011; Rampal et al., 2019). Wider adaption in traditional Eulerian sea-ice models may be hindered by numerical instabilities caused by rapid changes in ice strength (Lipscomb et al., 2007). Furthermore, current models are formulated under the continuum assumption where model cell sizes by far exceed the size of individual ice floes. While Roach et al. (2018) extended a continuum sea-ice model to prognostically determine the floe size distribution, ridging was not included due to the lack of a suitable physical description. Roberts et al. (2019) demonstrated with a variational principles and granular mechanics for the ice-rubble that macroporosity in ice ridges influences ridge mechanics and state.

As model resolutions increase, and potentially approach the size of large individual sea-ice floes, it becomes relevant to consider the physical basis for ridging on the ice-floe scale. Lagrangian particle-based sea ice models may be feasible alternatives to continuum models at high resolutions (e.g., Damsgaard et al., 2018; Gutfraind & Savage, 1997; Herman, 2016; Hopkins et al., 1991; Li et al., 2014), but still require model development for handling the multitude of involved physical phenomena. Lagrangian numerical models have been particularly effective at simulating the discontinuous evolution during ice ridging. Hopkins et al. (1991) simulated the compressive behavior of ice rubble with a particle-based numerical model, and concluded that the resultant increase in potential energy during ridge formation is a suitable metric for treating riding in large-scale models as long as the associated frictional losses were accounted for. Hopkins (2004) included a parameterization of ridging in a Lagrangian sea-ice model for the Arctic ocean. In this model, compressional strength linearly relaxes after ridging failure, and the internal stress distribution is reset every 24 h. However, the approach does not conform to physical principles of elasticity, plastic failure and frictional sliding.

Particle-based sea ice models are a useful tool for revisiting the idea of different failure stages in sea ice (Flato & Hibler, 1995; Tuhkuri & Lensu, 2002), as ice-floes are distinctively represented and can carry material properties along without problems of advective diffusion (e.g., Flato, 1993). In this study, we simulate the mechanics of two ice floes that undergo compressional strain and investigate the mechanical behavior before and after ridging is initiated. The transition between states is compared against an established threshold criterion (Amundrud et al., 2004). Based on these results, we derive a parameterization for larger-scale sea-ice models, and demonstrate how ridging mechanics influence larger-scale stress and strain distribution.

2. Methods

We model the sea-ice mechanics with a Lagrangian formulation based on the discrete-element method with breakable bonds (e.g., Cundall & Strack, 1979; Damsgaard et al., 2018; Potyondy & Cundall, 2004; Herman, 2016). The model is two-dimensional, with a horizontal (x) and a vertical axis (z). Each simulated ice

floe consists of many "ice particles," which are cylindrical units with separate kinematics. The translational momentum balance on each ice particle i is defined as,

$$m^i \frac{\mathrm{D}^2 \boldsymbol{x}^i}{\mathrm{D}t^2} = \underbrace{\sum_j \left(\boldsymbol{f}_{ij}^{\mathrm{n}} + \boldsymbol{f}_{ij}^{\mathrm{t}} \right)}_{\text{Contact forces}} + \boldsymbol{f}_{\mathrm{o}}^i + \boldsymbol{g} m^i + \boldsymbol{f}_{\mathrm{b}}^i. \tag{1}$$

The particle mass is m, and the vector $\boldsymbol{x}$ denotes spatial position of the particle center. Index j denotes other ice particles with mechanical interaction to particle i. Contact interaction is divided into force components normal ($\boldsymbol{f}_{\mathrm{n}}$) and tangential ($\boldsymbol{f}_{\mathrm{t}}$) to the contact orientation. Besides contact forces, a range of other components are included as body forces, here $\boldsymbol{f}_{\mathrm{o}}$ is ocean drag, $\boldsymbol{g}$ is gravitational acceleration, and a= $\rho_{\mathrm{w}} V_{\mathrm{s}}$ is buoyant uplift in water with density ρ_{w}. Ocean drag and buoyant uplift apply only to particles that are fully or partially submerged, and scale with relative submerged volume (V_{s}).

Similar to the translational momentum balance, the angular momentum balance for particle i is:

$$I_{\mathrm{y}}^i \frac{\mathrm{D}^2 \boldsymbol{\Omega}^i}{\mathrm{D}t^2} = \underbrace{\sum_j \left(r^i \boldsymbol{n}^{ij} \times \boldsymbol{f}_{ij}^{\mathrm{t}} \right)}_{\text{Contact torques}} + t_{\mathrm{o}}^i. \tag{2}$$

Here, I_y is the particle moment of inertia perpendicular to the simulation plane, Ω is the angular position, $\boldsymbol{n}$ is a normal vector to the plane of contact, and r is the particle radius. Drag torque t_{o} arises if the particle rotates relative to ocean vorticity. See Damsgaard et al. (2018) for further information on the force and torque components.

The momentum balance equations for ice-particle translation and rotation are explicitly integrated through time (t). The simulated ice-particle dynamics includes the full kinematic range from elastic wave propagation to plastic rearrangements.

2.1. Bonded Ice-Particle Mechanics

Interactions of bonded particles are simulated as elastic-plastic, that are based on beam theory, the 2D formulation of which was developed by Potyondy and Cundall (2004). Yield in ice is scale independent and can be described by Coulomb friction (e.g., Weiss & Schulson, 2009). We neglect ice viscous deformation as the characteristic Maxwell time for ice (MacAyeal & Sergienko, 2013; Maxwell, 1867) is several orders of magnitude longer than the duration of our two-floe compression experiments. The contact-normal force $\boldsymbol{f}_{\mathrm{n}}$ is given by:

$$\boldsymbol{f}_{\mathrm{n}}^{ij} = -A^{ij} E \boldsymbol{\delta}_{\mathrm{n}}^{ij}, \tag{3}$$

where $\boldsymbol{\delta}_{\mathrm{n}}$ is the relative displacement between ice particles, which can be compressive or tensile. E is Young's modulus of the contact, and A^{ij} is the contact cross-sectional area between the cylindrical elements, defined as:

$$A^{ij} = R^{ij} \min(h^i, h^j), \tag{4}$$

where $R^{\mathrm{ij}} = 2r^i r^j/(r^i + r^j)$ is the geometrical mean of the ice-particle radii, and h is particle thickness. The contact-tangential (parallel) force $\boldsymbol{f}_{\mathrm{t}}$ is defined as,

$$\boldsymbol{f}_{\mathrm{t}}^{ij} = -\frac{E A^{ij}}{R^{ij}} \frac{2(1-\nu^2)}{(2-\nu)(1+\nu)} \boldsymbol{\delta}_{\mathrm{t}}^{ij}, \tag{5}$$

where $\boldsymbol{\delta}_{\mathrm{t}}^{ij}$ is the tangential displacement vector on the contact interface. This displacement vector is incrementally calculated and corrected for contact rotation, in the same manner as done for unbonded-particle mechanics (Damsgaard et al., 2018). The magnitude of the bond-tangential force is limited by the Coulomb friction:

$$\| \boldsymbol{f}_{\mathrm{t}}^{ij} \| \leq \mu \| \boldsymbol{f}_{\mathrm{n}}^{ij} \| \tag{6}$$

The elastic-plastic bond formulation resists relative rotation, shear, and tension between ice particles, but bond can fail based on a strength criterion for each kinematic degree of freedom. The tensile stress on a particle-particle bond is limited by the ultimate tensile strength (σ_{uts}):

$$\sigma_{\mathrm{uts}} > \frac{\| \boldsymbol{f}_{\mathrm{n}}^{ij} \|}{A^{ij}} + \frac{| M_{\mathrm{t}}^{ij} | R^{ij}}{I^{ij}}, \tag{7}$$

where M_{t} is the bending momentum on the bond:

$$M_{\mathrm{t}}^{ij} = \frac{E}{r^i + r^j} I^{ij} \theta_{\mathrm{t}}^{ij}. \tag{8}$$

I^{ij} is the particle-pair moment of inertia, approximated as,

$$I^{ij} = \frac{2}{3} R_{ij}^3 \min(h_i, h_j), \tag{9}$$

and θ_{t} is the total relative rotation distance of the contact ($\theta_{\mathrm{t}}^{ij} = \int_t (\omega^j - \omega^i) dt$), with ω being particle angular velocity. The bond shear stress is limited by its shear strength σ_{s}:

$$\sigma_{\mathrm{s}} > \frac{\| \boldsymbol{f}_{\mathrm{t}}^{ij} \|}{A^{ij}}. \tag{10}$$

If the bond stresses (right-hand sides of Equations 7 and 10) exceed the prescribed strengths (σ_{uts} and σ_{s}), the bond fails and is removed from the simulation. Any further interaction between the ice-particle pair is governed by the cohesion-less and elastic-frictional mechanics described in Damsgaard et al. (2018).

3. Ice-Floe Compression Experiments and Limitations

3.1. Experiment Design

We simulate the mechanical interaction of two floating ice floes that are subjected to compression with a constant speed (Figure 1a). Each ice floe is constructed of many layers of ice particles arranged in a triangular packing, connected by elastic-plastic bonds. Ice viscosity can be neglected on the time scale of ridging, as the characteristic Maxwell time $t' = \eta/E$, with η being viscosity, is on the order of 100 days (Dansereau et al., 2017; MacAyeal & Sergienko, 2013; Maxwell, 1867). The outer edges of the ice floes are fixed horizontally but not vertically. The sea level is constant and the water is motionless. We vary the ice-floe geometries, compressional velocity, and numerical resolution between experiments. While our simulations do not include thermodynamics, we perform an additional experiment where we approximate the effects of instantaneous refreezing by forming new bonds between ice particles upon immediate contact. For comparison to existing analytical solutions used for sea-ice strength (Amundrud et al., 2004), we also model compressive mechanics of a floating, elastic sheet, as well as purely elastic-frictional ice floes with unbreakable bonds. The mechanical properties are in all cases uniform throughout the domain. The simulation parameters are listed in Table 1. We note that the chosen elastic modulus E actually relates to ice elasticity (Schulson, 1999), and is different to the elastic term in EVP-based continuum sea ice models that is included for numerical efficiency (e.g., Hunke, 2001; Lipscomb et al., 2007). Our compressional velocity is much faster than ridging in real sea-ice packs, but serves to decrease the computational costs for each experiment. It is common practice for discrete-element method simulations to use an accelerated forcing, as long as the acceleration keeps the elastic-frictional response rate-independent and pseudo static (e.g., Damsgaard et al., 2013; GDR-MiDi, 2004). Initial tests show that the inertial contribution to deformation is low, meaning that we can afford to use the shorter simulation duration while still obtaining the correct behavior.

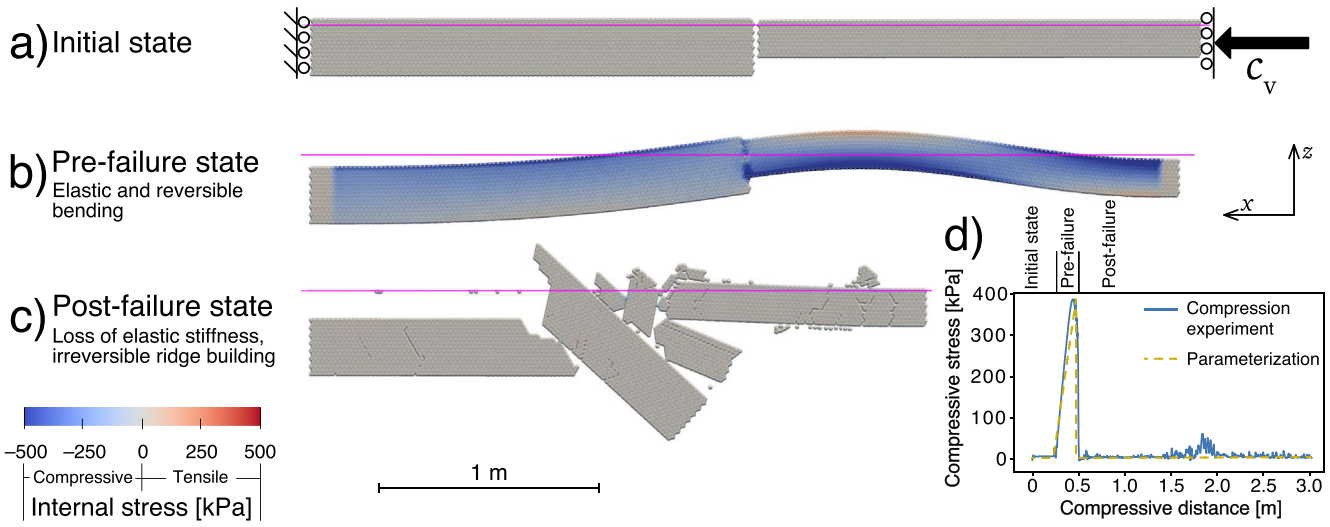

Figure 1. One of many ice-floe compression experiments with two elastic-plastic ice floes, each represented by a bonded grid of ice particles. The ice floes are seen from the side and colored according to the bond stresses. Time and compressive strain increases from panel (a) to (c), and the magenta horizontal lines denote sea level. (a) Ice floes are initialized so buoyancy equals gravitational pull, and are compressed with a constant velocity c_v. Compression causes elastic buckling (b) that under continued strain and brittle failure evolves to active ridging (c). The no-rotation boundary condition at the outer edges keeps the left ice floe submerged in (c) due to friction against the ice rubble in the center. (d) Measured stress during compression experiment compared to our parameterization (Equations 12–18).

3.2. Compression Experiment Results and Discussion

Figures 1b–1d shows the evolution of geometry and stresses during ice-floe compression. We divide the observed deformation behavior into two distinct states of pre and post-failure. The pre-failure state is characterized by elastic deformation through ice-floe internal stresses and geometric deflection (Figure 1b). At

Table 1
Simulation Parameters for Ice-Floe Compression Experiments

Parameter	Symbol	Value
Ice particle radii	r	0.010 m
Young's modulus	E	2.0×10^7 Pa
Poisson's ratio	ν	0.285
Coulomb friction coefficient	μ	0.30
Maximum bond tensile strength	σ_c	400 kPa
Maximum bond shear strength	σ_s	200 kPa
Compressive velocity	c_v	[0.05, 0.10, 0.2] m/s
Ice particle density	ρ_i	934 kg/m^3
Water density	ρ_w	1,000 kg/m^3
Length in no. of ice particles for left ice floe	$n_{x,1}$	100
Length in no. of ice particles for right ice floe	$n_{x,2}$	100
Thickness in no. of ice particles for left ice floe	$n_{z,1}$	[3, 5, 7, 9, 11, 13, 15, 17, 19, 21]
Thickness in no. of ice particles for right ice floe	$n_{z,2}$	[3, 5, 7, 9, 11, 13, 15, 17, 19, 21]
Gravitational acceleration	g_z	−9.8 m/s^2
Numerical time step length	Δt	8.48×10^{-6} s
Simulation length	t_{total}	$\frac{n_{x,1}+n_{x,2}}{2}\frac{2r}{c_v}$

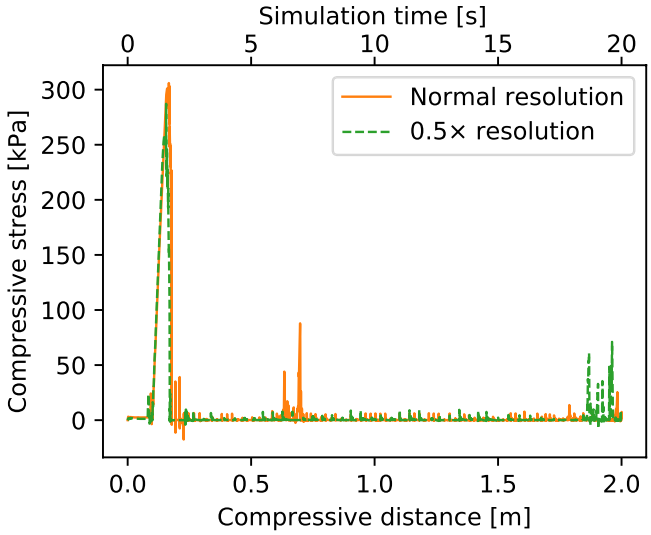

Figure 2. Analysis of simulation sensitivity to numerical resolution in two-floe compression experiment.

this point there is no plastic failure due to bond breakage, and the deformation is entirely elastic and reversible. Both ice floes experience large internal stresses during buckling, and compressive stress increases to a peak value (Figure 1d). Buckling is common when slender or thin materials are subjected to compressive stress, causing out-of-plane deflection and a reduction in elastic rigidity. While the applied forcing at the ice-floe scale is purely compressive, the ice-floe contact undergoes both compression and shear as a result of the buckling. The thinner ice floe buckles upwards, as the ice-floe contact center is situated above the midpoint of the thicker ice floe due to flotation. The geometric configuration creates a rotational moment at the floe-floe interface that bends the thinner ice floe up.

As compressive strain continues to increase, yield failure occurs in the zone of maximum curvature and tensile stress, here located at the top of the thinner ice floe (Figure 1b). After this point of peak stress, the floes enter a post-failure state where the ice floes are broken into smaller pieces in a disorganized pressure ridge (Figure 1c). The contact forces between ice particles in the pressure ridge are caused by gravity and buoyancy. Further compressional strain faces resistance by Coulomb frictional sliding in the ice rubble, which increases the potential energy during keel and sail construction. However, the bulk frictional resistance is during onset of the post-failure state smaller than the peak elastic stresses in the pre-failure state (Figure 1d). We note that structural weaknesses in the ice floes may dominate the failure patterns observed in our experiments containing uniform bond strength. Similarly, strength and geometrical variations in the third dimension may provide more gradual yield failure, but this is outside of our current simulation capabilities.

The modeled bond elasticity and strength scales with ice-particle size (Equation 4), and we verify that the observed behavior is not dependent of numerical resolution in the ice floes (Figure 2). Instantaneous refreezing between ice particles does not influence the peak stress values during the pre-failure state, but causes larger compressive strength in the post-failure state as the ice-rubble quickly gains cohesion (Figure 3). However, the structural rigidity is still much lower than in the pre-failure state, at least for the compressive distance modeled here.

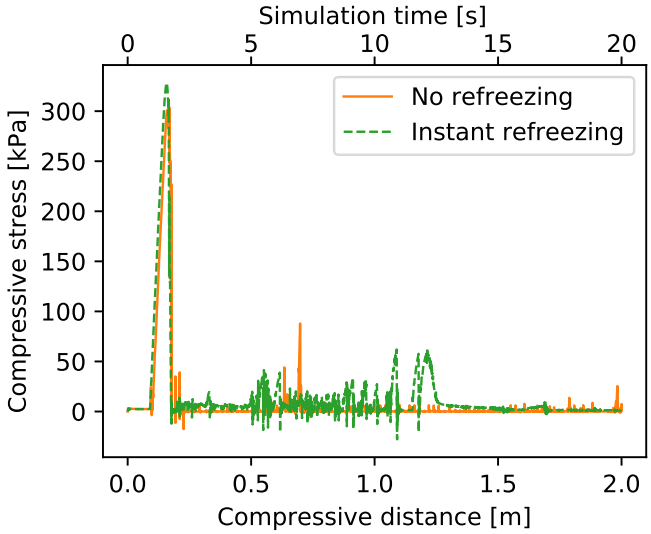

Figure 3. Comparison between regular two-floe compression experiment with no refreezing and experiment where ice-particle pairs instantaneously refreeze by gaining full bond strength upon contact.

For each ice-floe compression experiment, we plot the maximum observed compressive stress at the transition between pre and post-failure states (Figure 4). The maximum compressive stress increases with the thickness of the thinnest ice floe with a weak non-linearity. With uniform bond strength and elastic properties, the thickness of the thinnest ice floe controls the magnitude of the peak compressive stress with a weak non-linearity. When simulating an elastic sheet with unbreakable bonds instead of two elastic-plastic ice floes, our model reproduces the analytical ice-sheet buckling solution by Amundrud et al. (2004) (Figure 4). However, compared to the elastic-plastic ice floe compression experiments, our results show that the buckling solution for an elastic sheet is an overestimation of the ice rigidity. Therefore, we propose an empirical formulation for the maximum compressive strength in sea ice models that fits our experiments,

$$N_{\max} = K_{\mathrm{Ic}} \frac{\min(h_i, h_j)^{3/2}}{A^{ij}}, \tag{11}$$

where $N_{\max}$ is the maximum compressive stress before transitioning to the post-failure state, K_{Ic} is the fracture toughness of sea ice, $\min(h_i, h_j)$ is the thinnest ice thickness participating in the ridging, and A is the trans-

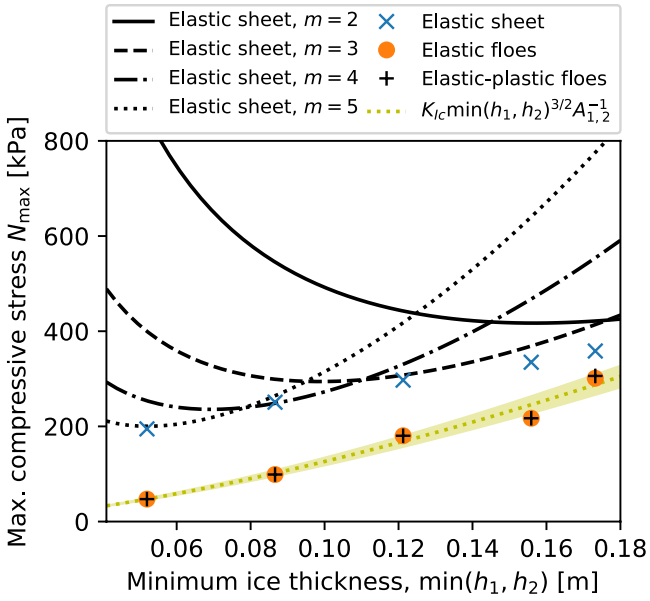

Figure 4. Peak compressive stresses in elastic (-plastic) ice floe and elastic sheet simulations, compared with analytical solutions for buckling stresses in elastic sheets (full lines, Equation 6 in Amundrud et al., 2004). The bending mode in the analytical solution is denoted m.

verse contact area (Equation 4, Figure 7a). The relationship implies that thinner ice floes in a multi-thickness assemblage are likely to ridge before thicker floes. Moreover, the relationship between ice thickness and ridging participation is not linear, as is commonly assumed (e.g., Hibler, 1979; Lipscomb et al., 2007), but with a exponent of 3/2, as suggested by Hibler (1980) and Hopkins (1998).

We fit Equation 11 to ice-floe peak strength from our compression experiments in Figure 4. A fracture toughness of 3.96×10^6 Pa m$^{1/2}$ provides the best correspondence to our simulation parameters (Table 1). In comparison, a commonly used value for sea-ice fracture toughness is 1.285×10^6 Pa m$^{1/2}$ (Hopkins, 2004), so our choices of bond shear and tensile strength are on the right order, but can be adjusted to approximate observed ridging dynamics.

Our initial compression simulations (Table 1, Figures 1–4) are by their geometry limited in cumulative compressive strain. We therefore perform an additional ice-floe compression experiment with six initial ice floes for the purpose of analyzing the resultant ice-thickness distribution with a more evolved ridge (Figure 5). The ice-thickness distribution displays exponential decrease (Figure 6), as characteristic for ridging-mechanics in real sea-ice packs (Godlovitch et al., 2011; Toppaladoddi & Wettlaufer, 2015). The thickness trend serves as a first-order validation of the model, but a thorough comparison to observations of ice distributions is not included due to the omission of thermodynamical processes.

4. Ridging Parameterization for Large-Scale Simulations

Large-scale particle sea-ice models have the potential to improve simulation of the marginal ice zone and other places where granular mechanics dominate the deformation (e.g., Damsgaard et al., 2018; Feltham, 2005; Gutfraind & Savage, 1997; Herman, 2016, 2017; Hopkins, 2004). On this scale, each particle typically represents a single ice floe, but a physically motivated ridging scheme is missing. We now parameterize the ice-contact mechanics observed in our two-floe compression experiments so that it can be applied to larger-scale particle models. Our parameterization does not include ice-thickness redistribution (e.g., Godlovitch et al., 2011; Roberts et al., 2019), but the mechanical parameterization is an important first step for particle sea-ice models.

Our simulated ice-floe interactions transition from an elastic and reversible pre-failure state, to a ridged or rafting post-failure state when mechanical failure and vertical redistribution of the ice mass changes the physics of interaction. We use the same model framework as for the two-floe compression experiment, but oriented the simulation space to plan view at the sea surface. Ice floes are defined to have constant vertical position, so we neglect the balance between gravitational pull and buoyancy (Equation 1). However, we introduce a compressive failure limit on the contact force between two ice floes i and j, based on the observed transition to pre and post-failure states (Equation 11 and Figure 4):

$$\| \boldsymbol{f}_{\mathrm{n}}^{ij} + \boldsymbol{f}_{\mathrm{t}}^{ij} \| \leq K_{\mathrm{Ic}} \min(h^i, h^j)^{3/2} \tag{12}$$

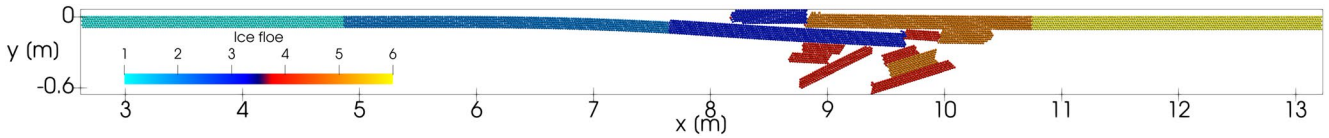

Figure 5. Ridge geometry at a compressive strain of $\epsilon_c = 0.33$ in an ice-floe compression experiment with six initial floes.

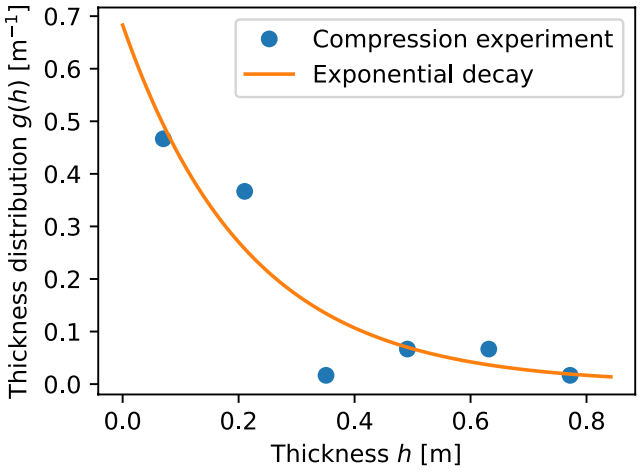

Figure 6. Points denote the modeled ice-thickness distribution in the ice-floe experiment in Figure 5. The blue line shows a fitted function of exponential decrease ($\alpha \exp(-h/\beta)$ where $\alpha = 0.68$ m^{-1} and $\beta = 0.22$ m).

Note that the orthogonal normal ($\boldsymbol{f}_n$) and tangential contact forces ($\boldsymbol{f}_t$) both can contribute to the compressive stress on the contact, which allows ridging to occur through both compression and shear (e.g., Schulson, 2004). The 3/2-order dependency between thickness and strength is consistent with some previous parameterizations of ridging failure (e.g., Hopkins, 1998; Rothrock, 1975), but not the commonly used linear relationship (e.g., Hibler, 1979).

Different from usual discrete-element methods, the compressive failure criterion (Equation 12) limits the compressive stresses between particles. If failure occurs, the contact mechanics on the ice-floe pair are replaced by elastic resistance to relative motion, limited by Coulomb friction on the contact surface. The contact surface is determined from the overlap extent and ice-floe shape, and the ice floes are assumed to undergo stacking as a means of vertical mass rearrangement (Figure 7b). The normal stress on the contact interface $\boldsymbol{\sigma}_n$ is determined by the hydrostatic response due to density differences and buoyancy:

$$\boldsymbol{\sigma}_n^{ij} = (\rho_w - \rho_i)(h_i + h_j)\boldsymbol{g}, \tag{13}$$

where ρ_w and ρ_i are the densities of water and ice, respectively, and $\boldsymbol{g}$ is the gravitational acceleration. The interficial tangential stress $\boldsymbol{\sigma}_t$ is sub-horizontal, and is determined by the horizontal sliding distance $\boldsymbol{\delta}_s$ and the interface area A (Figure 7b):

$$\boldsymbol{\sigma}_t^{ij} = -k_t \boldsymbol{\delta}_s^{ij} A_{ij}^{-1}. \tag{14}$$

The tangential contact stiffness k_t is found from the elastic parameters and contact-surface size (Obermayr et al., 2011):

$$k_t = \frac{2EA^{ij}(1-\nu^2)}{(2-\nu)(1+\nu)}, \tag{15}$$

where ν is Poisson's ratio. We uphold the Coulomb-frictional limit on the contact interface:

$$\| \boldsymbol{\sigma}_t^{ij} \| \leq \mu \| \boldsymbol{\sigma}_n^{ij} \|, \tag{16}$$

and excess elastic energy is recorded as frictional heat loss. Increases in contact strength by freezing can be added to the right-hand side of the above equation through a time and temperature-dependent cohesion term (e.g., Azarnejad & Brown, 2001), but is not included here. The normal and tangential forces on the ice floes for the momentum equations (Equations 1 and 2) are found by decomposing the tangential stress according to the contact orientation:

$$\boldsymbol{f}_n^{ij} = (\boldsymbol{\sigma}_t^{ij} \cdot \hat{\boldsymbol{n}}^{ij})A^{ij}, \tag{17}$$

and

$$\boldsymbol{f}_t^{ij} = (\boldsymbol{\sigma}_t^{ij} \cdot \hat{\boldsymbol{t}}^{ij})A^{ij}, \tag{18}$$

where $\hat{\boldsymbol{n}}$ and $\hat{\boldsymbol{t}}$ are unit-length normal and tangential vectors for the i and j particle pair. The above sliding forces grow non-linearly during compression as the overlap distance increases (Figure 7b).

We compare the ridging parameterization to the detailed elastic-plastic compressional experiments (Figure 1d), and the proposed parameterization captures the pre to post-state stress transition and stress magnitude in an adequate manner. The non-monotonic stress-strain behavior introduced here agrees with laboratory observations (Tuhkuri & Lensu, 2002), but is in contrast to the conventional approach where ice-pack

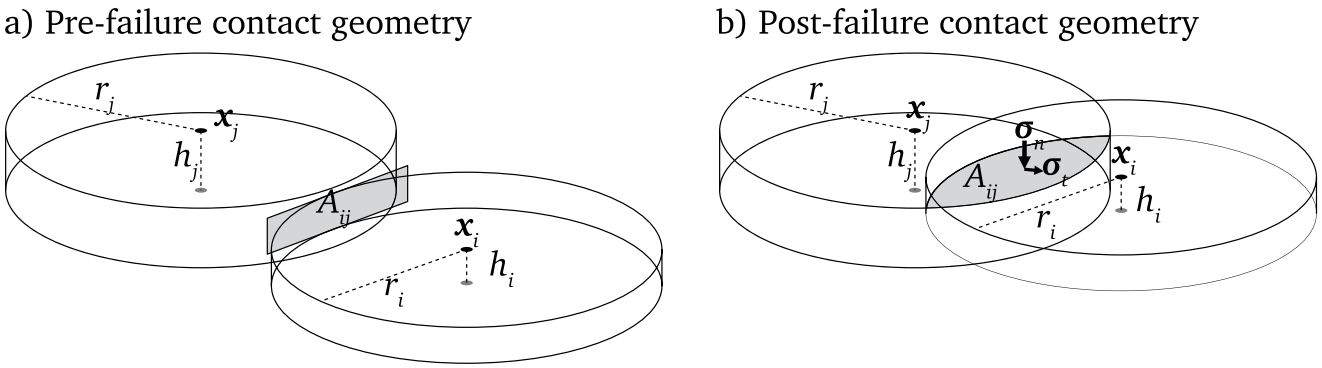

Figure 7. Simplified contact geometry for ice-floe pairs in particle-based sea-ice models, including transition from an original, pre-failure state (a), to an actively ridging mode in the post-failure state (b).

thickness alone governs the compressive sea-ice strength where no distinction is made between intact and actively ridging ice (e.g., Hibler, 1979; Rothrock, 1975).

4.1. Large-Scale Ridging Simulation Results

To assess the influence of the observed ridging dynamics on the bulk properties of an assemblage of many ice-floes, we generate cylindrical ice floes with diameters randomly chosen between 40 and 200 m. In these larger-scale experiments, each ice particle represents a single ice floe, and all ice floes have a thickness of 1 m. The elastic and frictional parameters are identical to the two-floe compression experiment (Table 1). We vary the fracture toughness (K_{Ic}) in the parameterized riding criterion (Equation 12) with two orders of magnitude, from 1.285×10^5 Pa m$^{1/2}$ to 1.285×10^7 Pa m$^{1/2}$. The right boundary ($-y$) of each run is moved at a constant velocity $c_v = 0.1$ m/s toward the left. The left boundary ($+y$) is fixed, and the top and bottom (x) boundaries are periodic.

Figure 8 shows the deformation behavior across the population of ice floes for three values of fracture toughness. At the onset of each experiment, the ice-floe assemblage is loosely packed, and the bulk compressive stress is here contributed by drag between ice and ocean. As a dense contact network forms at a compressive

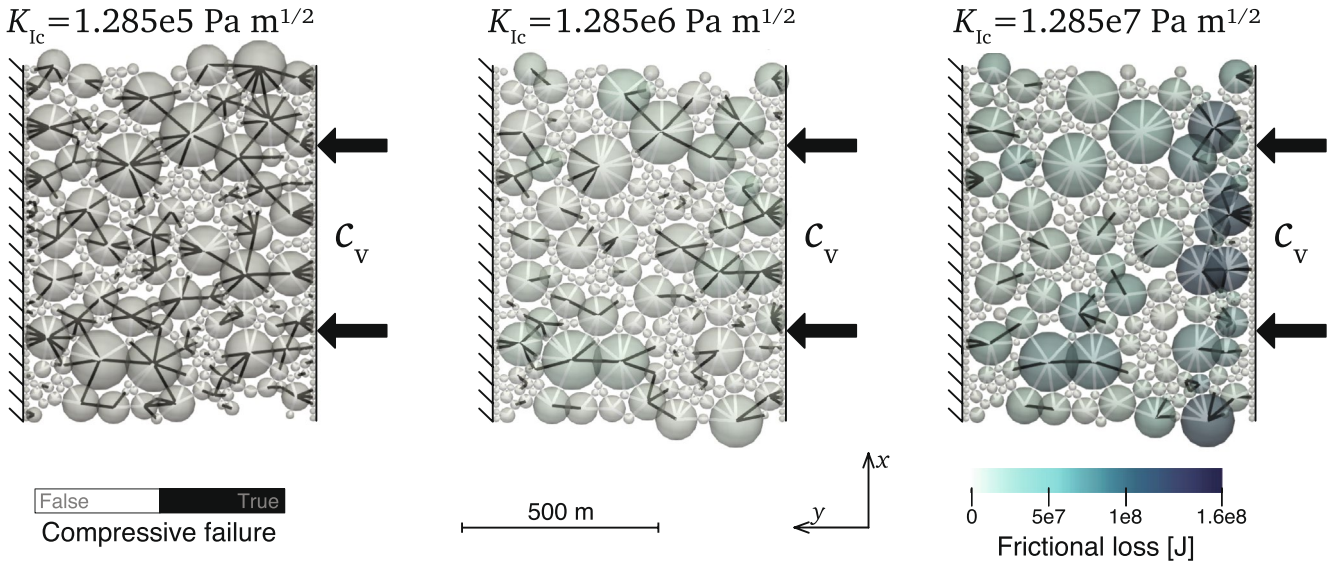

Figure 8. Uniaxial compression experiments at a compressive strain of $\epsilon_c = 0.45$. Ice floes are colored according to their thermal energy increase contributed by pre and post-failure contact sliding. Contacts between ice floes are marked by straight lines. White lines denote contacts in the pre-failure state, while black lines denote failure and active ridging. K_{Ic} is the fracture toughness value for each experiment, and c_v is the compressive velocity.

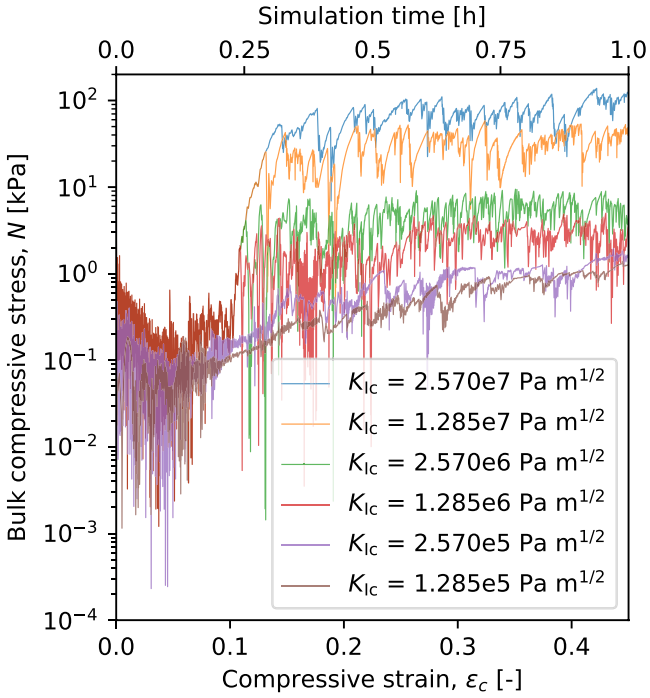

Figure 9. Bulk strength during uniaxial compression experiments with different fracture toughness (K_{Ic}) values.

strain of 0.1, elastic and frictional interactions from floe-floe collisions greatly increase the bulk compressive stress. The bulk compressive stress is in each case limited through the onset of ridging, scaled by the fracture toughness. With low fracture toughnesses ($K_{Ic} = 1.285 \times 10^5$ Pa m$^{1/2}$), the deformation is distributed and the majority of ice-floe contacts are actively ridging in the post-failure state. With higher fracture toughnesses, less contacts ridge and deformation is more localized. The frictional energy losses are higher and constrained to a few ice floes experiencing ridging. Larger ice floes are more likely to ridge than smaller ice floes, due to their larger circumference and role in the granular stress network. Stress localization in large grains is well known from simple granular materials (e.g., Voivret et al., 2009).

The bulk compressive strength of each ice-floe assemblage is heavily influenced by the magnitude of the fracture toughness (Figure 9). Low fracture toughness values cause a low bulk compressive stress as ice floes soon reach the relatively weak post-failure state with active ridging. The bulk assemblage strengthens with higher fracture toughness values, and individual ridging events cause significant temporary reductions in the bulk compressive stress. Failure events between ice floes cause stick-slip dynamics due to the rapid loss in contact strength.

5. Discussion and Conclusions

Sea ice ridging increases ice-pack thickness, and plays an important role in the formation of multi-year ice. Present sea-ice models use an assumption that compressive stress monotonically increases during compression. However, results of a high-resolution Lagrangian model used in this study show that the deformation is characterized by two distinct states, as also observed in laboratory ice compression experiments (Tuhkuri & Lensu, 2002). One is reversible elastic deformation, and the other one is irreversible brittle failure and ridge building. When ridging is initiated the compressive stress decreases by more than two orders of magnitude. The low compressional failure during ridge building is controlled by Coulomb sliding, buoyancy, and potential energy increase. The transient mechanical interactions are in direct contrast to sea-ice models that determine compressive stress from ice thickness alone, without distinguishing between ridging and non-ridging mechanics. Based on results of the Lagrangian-particle model simulations we propose to parameterize the observed behavior based on fracture toughness and Coulomb sliding, suitable for simulating ridging in particle-based sea-ice models. Elastic strength before failure depends on the ice thickness to a power of 3/2. In assemblages of many ice floes the mechanical transition and associated weakening causes stick-slip dynamics and strain localization, particularly with higher fracture toughness values. The proposed parameterization of elastic deformation and brittle failure effects on strength can be implemented in large-scale particle and continuum based sea-ice models. In particular, it is a step toward including ridging as a mechanism influencing not only sea-ice thickness and strength, but also the floe-size distribution (Roach et al., 2018). The parameterization potentially improves formation and dynamics of damaged zones, and consequently fidelity in representation of sea-ice state in climate models.

Data Availability Statement

Code availability simulations are performed with Granular.jl version 0.4.3, permanently archived at doi:10.5281/zenodo.4023858 (Damsgaard, 2020). Granular.jl is further developed at https://src.adamsgaard.dk/Granular.jl. All figures can be reproduced from the simulation scripts permanently archived at doi:10.5281/zenodo.3471354 (Damsgaard, 2019).

Acknowledgments
This work was supported by Exxon-Mobil through its membership in the Princeton E-filliates Partnership of the Andlinger Center for Energy and the Environment. Anders Damsgaard benefited from discussions with Mitchell Bushuk, Michael Winton, Cecilia Bitz, and Bruno Tremblay in preparation for this paper. We thank editors Robert Pincus and Sophie Nowicki for their assistance during the review process. We are indebted to four anonymous reviewers whose constructive comments greatly improved the manuscript.

References

Amundrud, T. L., Melling, H., & Ingram, R. G. (2004). Geometrical constraints on the evolution of ridged sea ice. *Journal of Geophysical Research*, *109*(C6), C06005. https://doi.org/10.1029/2003jc002251

Azarnejad, A., & Brown, T. G. (2001). Ice rubble behavior in punch tests. *Journal of Cold Regions Engineering*, *15*(3), 135–153. https://doi.org/10.1061/(asce)0887-381x10.1061/(asce)0887-381x(2001)15:3(135)

Batrak, Y., & Müller, M. (2018). Atmospheric response to kilometer-scale changes in sea ice concentration within the marginal ice zone. *Geophysical Research Letters*, *45*(13), 6702–6709. https://doi.org/10.1029/2018gl078295

Blanchard-Wrigglesworth, E., Barthélemy, A., Chevallier, M., Cullather, R., Fučkar, N., Massonnet, F., et al. (2016). Multi-model seasonal forecast of Arctic sea-ice: Forecast uncertainty at pan-Arctic and regional scales. *Climate Dynamics*, *49*(4), 1399–1410. https://doi.org/10.1007/s00382-016-3388-9

Bushuk, M., Msadek, R., Winton, M., Vecchi, G. A., Gudgel, R., Rosati, A., & Yang, X. (2017). Skillful regional prediction of Arctic sea ice on seasonal timescales. *Geophysical Research Letters*, *44*(10), 4953–4964. https://doi.org/10.1002/2017gl073155

Chiang, J. C. H., & Bitz, C. M. (2005). Influence of high latitude ice cover on the marine Intertropical Convergence Zone. *Climate Dynamics*, *25*(5), 477–496. https://doi.org/10.1007/s00382-005-0040-5

Coon, M. (1974). Mechanical behavior of compacted Arctic ice floes. *Journal of Petroleum Technology*, *26*(04), 466–470. https://doi.org/10.2118/3956-pa

Cundall, P. A., & Strack, O. D. L. (1979). A discrete numerical model for granular assemblies. *Géotechnique*, *29*, 47–65. https://doi.org/10.1680/geot.1979.29.1.47

Curry, J. A., Schramm, J. L., & Ebert, E. E. (1995). Sea ice-albedo climate feedback mechanism. *Journal of Climate*, *8*(2), 240–247. https://doi.org/10.1175/1520-0442(1995)008⟨0240:siacfm⟩2.0.co;2

Damsgaard, A. (2019). *Simulation scripts for ridging experiments with Granular.jl*. Zenodo. https://doi.org/10.5281/zenodo.3471354

Damsgaard, A. (2020). *Granular.jl v0.4.3: Granular dynamics simulation for Julia*. Zenodo. https://doi.org/10.5281/zenodo.4023858

Damsgaard, A., Adcroft, A., & Sergienko, O. (2018). Application of discrete-element methods to approximate sea-ice dynamics. *Journal of Advances in Modeling Earth Systems*, *10*(9), 2228–2244. https://doi.org/10.1029/2018MS001299

Damsgaard, A., Egholm, D. L., Piotrowski, J. A., Tulaczyk, S., Larsen, N. K., & Tylmann, K. (2013). Discrete element modeling of subglacial sediment deformation. *Journal of Geophysical Research: Earth Surface*, *118*, 2230–2242. https://doi.org/10.1002/2013JF002830

Dansereau, V., Weiss, J., Saramito, P., & Lattes, P. (2016). A Maxwell elasto-brittle rheology for sea ice modeling. *The Cryosphere*, *10*(3), 1339–1359. https://doi.org/10.5194/tc-10-1339-2016

Dansereau, V., Weiss, J., Saramito, P., Lattes, P., & Coche, E. (2017). Ice bridges and ridges in the maxwell-EB sea ice rheology. *The Cryosphere*, *11*(5), 2033–2058. https://doi.org/10.5194/tc-11-2033-2017

Day, J. J., Hawkins, E., & Tietsche, S. (2014). Will Arctic sea ice thickness initialization improve seasonal forecast skill? *Geophysical Research Letters*, *41*(21), 7566–7575. https://doi.org/10.1002/2014gl061694

Feltham, D. L. (2005). Granular flow in the marginal ice zone. *Philosophical Transactions of the Royal Society A*, *363*(1832), 1677–1700. https://doi.org/10.1098/rsta.2005.1601

Flato, G. M. (1993). A particle-in-cell sea-ice model. *Atmosphere-Ocean*, *31*(3), 339–358. https://doi.org/10.1080/07055900.1993.9649475

Flato, G. M., & Hibler, W. D. (1995). Ridging and strength in modeling the thickness distribution of Arctic sea ice. *Journal of Geophysical Research*, *100*(C9), 18611. https://doi.org/10.1029/95jc02091

GDR-MiDi. (2004). On dense granular flows. *European Physical Journal E*, *14*, 341–365. https://doi.org/10.1140/epje/i2003-10153-0

Girard, L., Bouillon, S., Weiss, J., Amitrano, D., Fichefet, T., & Legat, V. (2011). A new modeling framework for sea-ice mechanics based on elasto-brittle rheology. *Annals of Glaciology*, *52*(57), 123–132. https://doi.org/10.3189/172756411795931499

Godlovitch, D., Illner, R., & Monahan, A. (2011). Smoluchowski coagulation models of sea ice thickness distribution dynamics. *Journal of Geophysical Research*, *116*(C12), C12005. https://doi.org/10.1029/2011jc007125

Gutfraind, R., & Savage, S. B. (1997). Marginal ice zone rheology: Comparison of results from continuum-plastic models and discrete-particle simulations. *Journal of Geophysical Research*, *102*(C6), 12647–12661. https://doi.org/10.1029/97jc00124

Haas, C. (2003). Dynamics versus thermodynamics: The sea ice thickness distribution. In *Sea Ice*. Blackwell Science Ltd. (pp. 82–111). https://doi.org/10.1002/9780470757161.ch3

Heinonen, J. (2004). *Constitutive modeling of ice rubble in first-year ridge keel*. VTT Technical Research Centre of Finland. [G4 Monografiaväitöskirja]. Retrieved from http://urn.fi/urn:nbn:fi:tkk-001667

Herman, A. (2013). Shear-jamming in two-dimensional granular materials with power-law grain-size distribution. *Entropy*, *15*(11), 4802–4821. https://doi.org/10.3390/e15114802

Herman, A. (2016). Discrete-element bonded-particle sea ice model DESIgn, version 1.3a – model description and implementation. *Geoscientific Model Development*, *9*(3), 1219–1241. https://doi.org/10.5194/gmd-9-1219-2016

Herman, A. (2017). Wave-induced stress and breaking of sea ice in a coupled hydrodynamic discrete-element wave–ice model. *The Cryosphere*, *11*(6), 2711–2725. https://doi.org/10.5194/tc-11-2711-2017

Hibler, W. D. (1979). A dynamic thermodynamic sea ice model. *Journal of Physical Oceanography*, *9*(4), 815–846. https://doi.org/10.1175/1520-0485(1979)009⟨0815:adtsim⟩2.0.co;2

Hibler, W. D. (1980). Modeling a variable thickness sea ice cover. *Monthly Weather Review*, *108*(12), 1943–1973. https://doi.org/10.1175/1520-0493(1980)108⟨1943:mavtsi⟩2.0.co;2

Holland, M. M., Serreze, M. C., & Stroeve, J. (2010). The sea ice mass budget of the arctic and its future change as simulated by coupled climate models. *Climate Dynamics*, *34*(2–3), 185–200. https://doi.org/10.1007/s00382-008-0493-4

Hopkins, M. A. (1994). On the ridging of intact lead ice. *Journal of Geophysical Research*, *99*(C8), 16351. https://doi.org/10.1029/94jc00996

Hopkins, M. A. (1998). Four stages of pressure ridging. *Journal of Geophysical Research*, *103*(C10), 21883–21891. https://doi.org/10.1029/98jc01257

Hopkins, M. A. (2004). A discrete element Lagrangian Sea ice model. *Engineering Computations*, *21*(2/3/4), 409–421. https://doi.org/10.1108/02644400410519857

Hopkins, M. A., Hibler, W. D., & Flato, G. M. (1991). On the numerical simulation of the sea ice ridging process. *Journal of Geophysical Research*, *96*(C3), 4809. https://doi.org/10.1029/90jc02375

Hopkins, M. A., Tuhkuri, J., & Lensu, M. (1999). Rafting and ridging of thin ice sheets. *Journal of Geophysical Research*, *104*(C6), 13605–13613. https://doi.org/10.1029/1999jc900031

Hunke, E. C. (2001). Viscous–plastic sea ice dynamics with the EVP model: Linearization issues. *Journal of Computational Physics*, *170*(1), 18–38. https://doi.org/10.1006/jcph.2001.6710

Li, B., Li, H., Liu, Y., Wang, A., & Ji, S. (2014). A modified discrete element model for sea ice dynamics. *Acta Oceanologica Sinica*, *33*(1), 56–63. https://doi.org/10.1007/s13131-014-0428-3

Lindsay, R. W., Zhang, J., Schweiger, A. J., & Steele, M. A. (2008). Seasonal predictions of ice extent in the Arctic ocean. *Journal of Geophysical Research*, *113*(C2), C02023. https://doi.org/10.1029/2007jc004259

Lipscomb, W. H., Hunke, E. C., Maslowski, W., & Jakacki, J. (2007). Ridging, strength, and stability in high-resolution sea ice models. *Journal of Geophysical Research*, *112*(C3), C03S91. https://doi.org/10.1029/2005jc003355

MacAyeal, D. R., & Sergienko, O. V. (2013). The flexural dynamics of melting ice shelves. *Annals of Glaciology*, *54*(63), 1–10. https://doi.org/10.3189/2013aog63a256

Maxwell, J. C. (1867). On the dynamical theory of gases. *Philosophical Transactions of the Royal Society of London*, *157*, 49–88. https://doi.org/10.1098/rstl.1867.0004

Mellor, M. (1980). Ship resistance in thick brash ice. *Cold Regions Science and Technology*, *3*(4), 305–321. https://doi.org/10.1016/0165-232x(80)90037-3

Obermayr, M., Dressler, K., Vrettos, C., & Eberhard, P. (2011). Prediction of draft forces in cohesionless soil with the discrete element method. *Journal of Terramechanics*, *48*(5), 347–358. https://doi.org/10.1016/j.jterra.2011.08.003

Parmerter, R. R. (1975). A model of simple rafting in sea ice. *Journal of Geophysical Research*, *80*(15), 1948–1952. https://doi.org/10.1029/jc080i015p01948

Parmerter, R. R., & Coon, M. D. (1973). On the mechanics of pressure ridge formation in sea ice. In *Offshore technology conference*. https://doi.org/10.4043/1810-ms

Potyondy, D. O., & Cundall, P. A. (2004). A bonded-particle model for rock. *International Journal of Rock Mechanics and Mining Sciences*, *41*(8), 1329–1364. https://doi.org/10.1016/j.ijrmms.2004.09.011

Pritchard, R. S. (1975). An elastic-plastic constitutive law for sea ice. *Journal of Applied Mechanics*, *42*(2), 379–384. https://doi.org/10.1115/1.3423585

Rallabandi, B., Zheng, Z., Winton, M., & Stone, H. A. (2017). Formation of sea ice bridges in narrow straits in response to wind and water stresses. *Journal of Geophysical Research: Oceans*, *122*(7), 5588–5610. https://doi.org/10.1002/2017jc012822

Rampal, P., Dansereau, V., Olason, E., Bouillon, S., Williams, T., Korosov, A., & Samaké, A. (2019). On the multi-fractal scaling properties of sea ice deformation. *The Cryosphere*, *13*(9), 2457–2474. https://doi.org/10.5194/tc-13-2457-2019

Roach, L. A., Horvat, C., Dean, S. M., & Bitz, C. M. (2018). An emergent sea ice floe size distribution in a global coupled ocean-sea ice model. *Journal of Geophysical Research: Oceans*, *123*(6), 4322–4337. https://doi.org/10.1029/2017jc013692

Roberts, A. F., Hunke, E. C., Kamal, S. M., Lipscomb, W. H., Horvat, C., & Maslowski, W. (2019). A variational method for sea ice ridging in earth system models. *Journal of Advances in Modeling Earth Systems*, *11*(3), 771–805. https://doi.org/10.1029/2018ms001395

Rothrock, D. A. (1975). The energetics of the plastic deformation of pack ice by ridging. *Journal of Geophysical Research*, *80*(33), 4514–4519. https://doi.org/10.1029/jc080i033p04514

Schulson, E. M. (1999). The structure and mechanical behavior of ice. *JOM*, *51*(2), 21–27. https://doi.org/10.1007/s11837-999-0206-4

Schulson, E. M. (2004). Compressive shear faults within arctic sea ice: Fracture on scales large and small. *Journal of Geophysical Research*, *109*(C7), C07016. https://doi.org/10.1029/2003jc002108

Screen, J. A., & Simmonds, I. (2010). The central role of diminishing sea ice in recent Arctic temperature amplification. *Nature*, *464*(7293), 1334–1337. https://doi.org/10.1038/nature09051

Shen, H. T., & Liu, L. (2003). Shokotsu River ice jam formation. *Cold Regions Science and Technology*, *37*(1), 35–49. https://doi.org/10.1016/s0165-232x(03)00034-x

Thorndike, A. S., Rothrock, D. A., Maykut, G. A., & Colony, R. (1975). The thickness distribution of sea ice. *Journal of Geophysical Research*, *80*(33), 4501–4513. https://doi.org/10.1029/jc080i033p04501

Timco, G., Croasdale, K., & Wright, B. (2000). An overview of first-year sea ice ridges. *Canadian Hydraulics Centre Technical Report*. https://doi.org/10.4224/12327286

Toppaladoddi, S., & Wettlaufer, J. (2015). Theory of the sea ice thickness distribution. *Physical Review Letters*, *115*(14), 148501. https://doi.org/10.1103/physrevlett.115.148501

Tsamados, M., Feltham, D. L., Schroeder, D., Flocco, D., Farrell, S. L., Kurtz, N., et al. (2014). Impact of variable atmospheric and oceanic form drag on simulations of arctic sea ice. *Journal of Physical Oceanography*, *44*(5), 1329–1353. https://doi.org/10.1175/jpo-d-13-0215.1

Tuhkuri, J., & Lensu, M. (2002). Laboratory tests on ridging and rafting of ice sheets. *Journal of Geophysical Research*, *107*(C9), 3125. https://doi.org/10.1029/2001jc000848

Ungermann, M., Tremblay, L. B., Martin, T., & Losch, M. (2017). Impact of the ice strength formulation on the performance of a sea ice thickness distribution model in the arctic. *Journal of Geophysical Research: Oceans*, *122*, 2090–2107. https://doi.org/10.1002/2016JC012128

Voivret, C., Radjaï, F., Delenne, J.-Y., & El Youssoufi, M. S. (2009). Multiscale force networks in highly polydisperse granular media. *Physical Review Letters*, *102*, 178001. https://doi.org/10.1103/PhysRevLett.102.178001

Weiss, J., & Schulson, E. M. (2009). Coulombic faulting from the grain scale to the geophysical scale: Lessons from ice. *Journal of Physics D Applied Physics*, *42*(21), 214017. https://doi.org/10.1088/0022-3727/42/21/214017